CFHTLenS: testing the laws of gravity with tomographic weak lensing and redshift-space distortions

Fergus Simpson, Catherine Heymans, David Parkinson, Chris Blake, Martin Kilbinger, Jonathan Benjamin, Thomas Erben, Hendrik Hildebrandt, Henk Hoekstra, Thomas D. Kitching, et al.

Monthly Notices of the ROYAL ASTRONOMICAL SOCIETY

MNRAS **429,** 2249–2263 (2013) doi:10.1093/mnras/sts493

CFHTLenS: testing the laws of gravity with tomographic weak lensing and redshift-space distortions

Fergus Simpson,[1★] Catherine Heymans,[1] David Parkinson,[2] Chris Blake,[3] Martin Kilbinger,[4,5,6] Jonathan Benjamin,[7] Thomas Erben,[8] Hendrik Hildebrandt,[7,8] Henk Hoekstra,[9,10] Thomas D. Kitching,[1] Yannick Mellier,[11] Lance Miller,[12] Ludovic Van Waerbeke,[7] Jean Coupon,[13] Liping Fu,[14] Joachim Harnois-Déraps,[15,16] Michael J. Hudson,[17,18] Koenraad Kuijken,[9] Barnaby Rowe,[19,20] Tim Schrabback,[8,9,21] Elisabetta Semboloni,[9] Sanaz Vafaei[7] and Malin Velander[9,12]

[1] *Scottish Universities Physics Alliance, Institute for Astronomy, University of Edinburgh, Royal Observatory, Blackford Hill, Edinburgh EH9 3HJ*
[2] *School of Mathematics and Physics, University of Queensland, Brisbane, QLD 4072, Australia*
[3] *Centre for Astrophysics and Supercomputing, Swinburne University of Technology, PO Box 218, Hawthorn, VIC 3122, Australia*
[4] *CEA Saclay, Service d'Astrophysique (SAp), Orme des Merisiers, Bât 709, F-91191 Gif-sur-Yvette, France*
[5] *Excellence Cluster Universe, Boltzmannstr. 2, D-85748 Garching, Germany*
[6] *Universitäts-Sternwarte, Ludwig-Maximillians-Universität München, Scheinerstr. 1, D-81679 München, Germany*
[7] *Department of Physics and Astronomy, University of British Columbia, 6224 Agricultural Road, Vancouver, BC V6T 1Z1, Canada*
[8] *Argelander Institute for Astronomy, University of Bonn, Auf dem Hügel 71, D-53121 Bonn, Germany*
[9] *Leiden Observatory, Leiden University, Niels Bohrweg 2, NL-2333 CA Leiden, the Netherlands*
[10] *Department of Physics and Astronomy, University of Victoria, Victoria, BC V8P 5C2, Canada*
[11] *Institut d'Astrophysique de Paris, Université Pierre et Marie Curie – Paris 6, 98 bis Boulevard Arago, F-75014 Paris, France*
[12] *Department of Physics, Oxford University, Keble Road, Oxford OX1 3RH*
[13] *Institute of Astronomy and Astrophysics, Academia Sinica, PO Box 23-141, Taipei 10617, Taiwan*
[14] *Key Lab for Astrophysics, Shanghai Normal University, 100 Guilin Road, 200234 Shanghai, China*
[15] *Canadian Institute for Theoretical Astrophysics, University of Toronto, ON M5S 3H8, Canada*
[16] *Department of Physics, University of Toronto, ON M5S 1A7, Canada*
[17] *Department of Physics and Astronomy, University of Waterloo, Waterloo, ON N2L 3G1, Canada*
[18] *Perimeter Institute for Theoretical Physics, 31 Caroline Street N, Waterloo, ON N2L 1Y5, Canada*
[19] *Department of Physics and Astronomy, University College London, Gower Street, London WC1E 6BT*
[20] *California Institute of Technology, 1200 E California Boulevard, Pasadena, CA 91125, USA*
[21] *Kavli Institute for Particle Astrophysics and Cosmology, Stanford University, 382 Via Pueblo Mall, Stanford, CA 94305-4060, USA*

Accepted 2012 November 26. Received 2012 November 26; in original form 2012 September 4

ABSTRACT

Dark energy may be the first sign of new fundamental physics in the Universe, taking either a physical form or revealing a correction to Einsteinian gravity. Weak gravitational lensing and galaxy peculiar velocities provide complementary probes of general relativity, and in combination allow us to test modified theories of gravity in a unique way. We perform such an analysis by combining measurements of cosmic shear tomography from the Canada–France–Hawaii Telescope Lensing Survey (CFHTLenS) with the growth of structure from the WiggleZ Dark Energy Survey and the Six-degree-Field Galaxy Survey, producing the strongest existing joint constraints on the metric potentials that describe general theories of gravity. For scale-independent modifications to the metric potentials which evolve linearly with the effective dark energy density, we find present-day cosmological deviations in the Newtonian potential and curvature potential from the prediction of general relativity to be $\Delta\Psi/\Psi = 0.05 \pm 0.25$ and $\Delta\Phi/\Phi = -0.05 \pm 0.3$, respectively (68 per cent confidence limits).

Key words: gravitational lensing: weak – cosmology: observations.

★E-mail: frgs@roe.ac.uk

1 INTRODUCTION

Einstein's original formulation of general relativity (GR) provides a remarkably precise prescription for the motions of particles in our Solar system (Einstein 1916). It has survived close to a century of experimental scrutiny, beginning with the precession of Mercury's orbit and the gravitational deflection of starlight, progressing to ground-based tests with atomic clocks. Recent spaceborne tests now confirm certain predictions of GR to better than one part in 10 000 (Bertotti, Iess & Tortora 2003). However when we consider the behaviour of gravity on cosmological scales, which are over 14 orders of magnitude greater than the interplanetary distances, there is much greater scope for uncertainty. Observational evidence of an accelerating universe has called Einstein's laws into question. The underlying cause for this 'dark energy' phenomenon may lie within our current understanding of gravitational physics, the leading candidate being the cosmological constant. Another possibility is that a new regime of gravitational physics has been exposed. It is this prospect which has led to a recent flurry of activity in constraining the cosmological nature of gravity (Bean & Tangmatitham 2010; Daniel et al. 2010; Reyes et al. 2010; Zhao et al. 2010, 2012; Song et al. 2011; Tereno, Semboloni & Schrabback 2011; Hudson & Turnbull 2012; Rapetti et al. 2012; Samushia et al. 2012; Zuntz et al. 2012).

Much like in the Solar system, we are able to study the cosmological trajectories of both relativistic and non-relativistic particles, at least in a statistical sense. The peculiar motions of galaxies falling towards overdense regions generate an illusory anisotropy in their clustering pattern (Kaiser 1987), known as redshift-space distortions (RSDs). This effect has been observed with heightened precision over the past decade (Peacock et al. 2001; Hawkins et al. 2003; Guzzo et al. 2008; Blake et al. 2011; Beutler et al. 2012; Reid et al. 2012) permitting inferences of the rate at which cosmological structure forms. The peculiar velocities of galaxies can also be observed directly, and the inferred measurements of the growth rate are consistent with those from RSDs (see Hudson & Turnbull 2012, and references therein).

For gravitational experiments, relativistic test particles are of particular interest since their motions are not only sensitive to the effects of time dilation but also to the curvature of space. In the classical test of GR, the deflection of starlight was observed during a solar eclipse (Dyson, Eddington & Davidson 1920). In our experiment, distant galaxies replace nearby stars as the source of photons, our relativistic test particle. When imaging these distant galaxies, instead of measuring their gravitational deflection angles, which are unknown, we can study their shapes which appear correlated as a result of the gravitational deflection of light (Bartelmann & Schneider 2001).

One important caveat is that we are required to convert angles and redshifts into physical distances when interpreting observations of RSDs and gravitational lensing. We therefore require additional information on the geometry of the universe. Geometric measurements of dark energy such as supernovae and baryon acoustic oscillations (BAO), conventionally used to determine the equation of state for dark energy, $w(z)$, are crucial for this purpose. However their measurements alone cannot distinguish modified gravity models, which are in general capable of reproducing any given w cold dark matter (wCDM) expansion history. The cosmic microwave background (CMB) is also used to further break degeneracies, and provides a high-redshift anchor for the amplitude of density perturbations (see e.g. Komatsu et al. 2011).

Gravitational lensing is not unique in its ability to probe both metric potentials. CMB photons gain or lose energy as the potentials evolve, a phenomenon known as the Integrated Sachs–Wolfe (ISW) effect, leaving a significant anisotropy on the largest angular scales. In the context of a flat ΛCDM background, the expected signal strength from GR is modest, while many alternative theories of gravity can readily generate very large ISW signals, something which is not seen in the data (Lombriser et al. 2009; Zuntz et al. 2012).

While we currently lack a specific model which can compete with GR in terms of simplicity and physical motivation, there exist broad families of models such as $f(R)$ which provide useful test cases. For a recent review of the full menagerie of models, see Clifton et al. (2012). In this work we do not aim to constrain the parameter space of a particular family of models, or explicitly perform Bayesian model selection, but instead simply address the question of whether our data appear consistent with the predictions of GR. In addition to the cosmic shear data from the Canada–France–Hawaii Telescope Lensing Survey (CFHTLenS), we make use of RSDs from WiggleZ Dark Energy Survey (WiggleZ) and the Six-degree-Field Galaxy Survey (6dFGS).

In Section 2 we outline our choice of parametrization for departures from GR. Our data sets are summarized in Sections 3 and 4, followed by our methods and main results in Sections 5 and 6. A comparison with alternative parametrization schemes is presented in Section 7, and we briefly review the status of theoretical models of modified gravity in Section 8, with concluding remarks in Section 9.

2 PARAMETRIZING THE MODIFICATION

Given the lack of a compelling model to rival GR, we choose to parametrize deviations from GR in a phenomenological manner. In effect, we simply wish to ask: Is the strength of gravity the same on cosmological scales as it is here on Earth? If not, this may modify the motions of both relativistic and non-relativistic particles, but not necessarily in the same manner. Fig. 1 illustrates why we are seeking a modified gravity signal on cosmological scales; it is the regime in which the classical Newtonian attraction is overwhelmed by the repulsive force associated with dark energy.

The perturbed Friedmann–Robertson–Walker metric may be expressed in terms of the scale factor $a(t)$, the Newtonian potential Ψ and the curvature potential Φ:

$$\mathrm{d}s^2 = (1 + 2\Psi)\,\mathrm{d}t^2 - a^2(t)\,(1 - 2\Phi)\,\mathrm{d}\boldsymbol{x}^2. \tag{1}$$

In GR each of the two gravitational potentials Ψ and Φ, which carry implicit spatial and temporal dependencies, may be determined from the distribution of matter in the Universe. In Fourier space this is given by

$$k^2\Phi_{\rm GR} = -4\pi G a^2 \bar{\rho}\delta, \tag{2}$$

where we have introduced the wavenumber k, the mean cosmic density $\bar{\rho}$ and the fractional density perturbation $\delta \equiv \rho/\bar{\rho} - 1$. In the absence of anisotropic stress the two potentials are identical, $\Psi(x, t) = \Phi(x, t)$. Relativistic particles collect equal contributions from the two potentials, since they traverse equal quantities of space and time, such that

$$k^2\,(\Psi_{\rm GR} + \Phi_{\rm GR}) = -8\pi G a^2 \bar{\rho}\delta. \tag{3}$$

We wish to investigate deviations from GR with a general parametrization. Hereafter, each of the two probes, the Newtonian

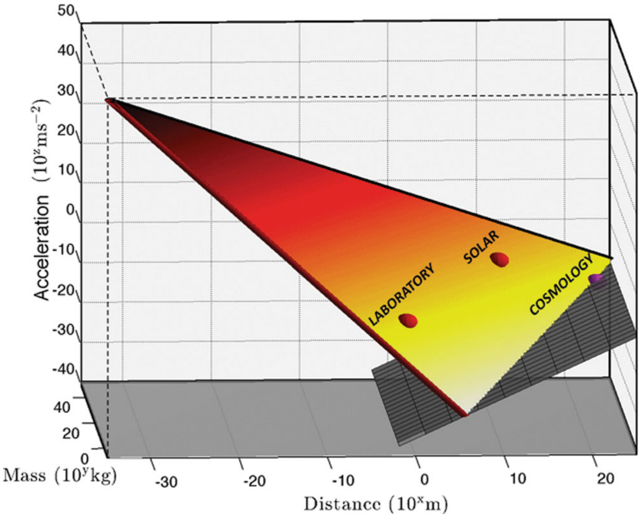

Figure 1. The shaded triangle represents the vast regime over which the gravitational acceleration of a test particle in the proximity of a mass M is thought to be well described by the Newtonian prescription $a = GMr^{-2}$. While torsion balance (laboratory) and space-based (Solar system) tests of gravity offer superior accuracy, cosmological methods push the boundaries of our understanding of gravity. For clarity we truncate the mass axis at the Planck mass (red edge), while the upper bound (black edge) denotes the Schwarzschild radius. The grey slope illustrates the amplitude of the negative contribution arising from dark energy, which scales in proportion to r, and surpasses the conventional Newtonian force at cosmological scales.

potential Ψ experienced by non-relativistic particles and the lensing potential $(\Phi + \Psi)$ experienced by relativistic particles, is now modulated by the parameters Σ and μ:

$$\Psi(k, a) = [1 + \mu(k, a)]\,\Psi_{\rm GR}(k, a), \tag{4}$$

$$[\Psi(k, a) + \Phi(k, a)] = [1 + \Sigma(k, a)]\,[\Psi_{\rm GR}(k, a) + \Phi_{\rm GR}(k, a)]\,, \tag{5}$$

where we have adopted notation similar to that of Amendola, Kunz & Sapone (2008), as used more recently by Zhao et al. (2010) and Song et al. (2011). This parametrization has the advantage of separating the modified behaviour of non-relativistic particles, as dictated by $\mu(k, a)$, from modifications to the deflection of light, as given by $\Sigma(k, a)$. By being able to reproduce a wide range of observational outcomes, in terms of the two-point weak lensing correlation functions and the growth of large-scale structure, we ensure a broad sensitivity to different types of deviations from GR. There is some flexibility in how we choose to parametrize the scale and time dependence of these two parameters, much like the dark energy equation of state $w(z)$. Previous works have often chosen a scale-independent model with a parametrized time variation of these functions such that $\Sigma(a) = \Sigma_{\rm s} a^{\rm s}$ and $\mu(a) = \mu_{\rm s} a^{\rm s}$. However given that our primary motivation for modified gravity is to seek an explanation of the dark energy phenomenon, we model the time evolution to scale in proportion with the effective dark energy density implied by the background dynamics, such that

$$\Sigma(a) = \Sigma_0 \frac{\Omega_\Lambda(a)}{\Omega_\Lambda}, \quad \mu(a) = \mu_0 \frac{\Omega_\Lambda(a)}{\Omega_\Lambda}, \tag{6}$$

where we have defined $\Omega_\Lambda \equiv \Omega_\Lambda(a = 1)$; this normalization was chosen such that μ_0 and Σ_0 reflect the present day values of $\mu(a)$ and $\Sigma(a)$, respectively. Note that for the case of GR, $\Sigma_0 = \mu_0 = 0$. One advantage of this parametrization is that it permits a trivial mapping between μ_0 and the popular growth index γ (Wang & Steinhardt 1998; Linder 2005). It also reduces the total number of degrees of freedom, thereby allowing us to maintain a manageable error budget. The disadvantage is that we become less sensitive to deviations from GR whose time evolution differs significantly from the adopted model. The lack of scale dependence in this model may seem questionable given the stringent Solar system tests which must be satisfied. However the length scales probed by our cosmological data sets are over 14 orders of magnitude greater, leaving ample opportunity for a transition at scales smaller than those studied here. Furthermore, any significant departure from scale-independent growth is more readily apparent from studies of the shape of the galaxy power spectrum.

With our modified potentials in equations (4) and (5) the growth of linear density perturbations is now given by

$$\delta''(a) + \left(\frac{2}{a} + \frac{\ddot{a}}{\dot{a}^2}\right)\delta'(a) - \frac{3\Omega_{\rm m}}{2a^2}\left[\boldsymbol{1 + \mu(a)}\right]\delta(a) = 0, \tag{7}$$

while the cosmic shear power spectrum $P_\kappa^{i,j}(\ell)$ correlating redshift bins i and j takes the form

$$P_\kappa^{i,j}(\ell) = \frac{9}{4}\Omega_{\rm m}^2 \left(\frac{H_0}{c}\right)^4 \int_0^\infty \frac{g_i(\chi) g_j(\chi)}{a^2(\chi)} P_\delta\left(\frac{\ell}{f_K(\chi)}, \chi\right) \times \boldsymbol{[1 + \Sigma(\chi)]^2}\,{\rm d}\chi, \tag{8}$$

where the terms not present in the equations' conventional form are highlighted in bold. Here χ denotes the radial coordinate distance, while f_K is the comoving angular diameter distance. Note also that $P_\kappa(\ell)$ possesses an implicit dependence on μ via the time evolution of the P_δ term. The lensing efficiency g_i is determined by the radial distribution of source galaxies $n_i(\chi)$ and the comoving angular diameter distance $f_K(\chi)$:

$$g_i(\chi) = \int_\chi^\infty {\rm d}\chi' n_i(\chi') \frac{f_K(\chi' - \chi)}{f_K(\chi')}. \tag{9}$$

Note that our parameters μ_0 and Σ_0 are only modulating the gravitational potentials in equation (1), but not the evolution of the expansion $a(t)$. The standard cosmological model, in the form of a flat ΛCDM universe, is known to provide a good description of the cosmic geometry, therefore for most of this paper we work on the assumption of this global expansion, and focus on exploring the less well determined behaviour of the gravitational perturbations. We shall also explore the consequences of adding further degrees of freedom to the expansion history, in the form of an effective dark energy equation of state w and the global curvature Ω_K.

3 GEOMETRIC DATA

When considering the prospect of modified gravity, we must relax the assumption that light deflection and structure formation follow the predictions of GR. This significantly exacerbates the task of constraining all of our unknown cosmological parameters. For example, without knowing how mass bends light on cosmological scales, we cannot hope to use gravitational lensing to measure the geometry of the Universe. We therefore require auxiliary data to assist in measuring the conventional cosmological parameters, those which govern the cosmic expansion history and shape of the matter power spectrum, before we can attempt to tackle the gravitational parameters μ_0 and Σ_0.

3.1 Hubble parameter

The current rate of cosmological expansion has long been a source of great uncertainty, largely due to the inherent difficulty in performing distance measurements. Considerable improvements have been made in the past decade, and we make use of a recent result obtained from combining observations of local supernovae, Cepheid variables and the megamaser at the centre of NGC 4258 (Riess et al. 2011). Where stated, we include a Gaussian prior $H_0 = 73.8 \pm 2.4\,\mathrm{km\,s^{-1}\,Mpc^{-1}}$ from Riess et al. (2011). In de Sitter space this would correspond to the distance between any two comoving points doubling every 13 billion years.

Since it is common practice to assume GR in most astronomical and cosmological studies, extra care must be taken when adopting quoted results from previous studies. For example, the determination of the distance to water masers is based on the assumption of Keplerian motions. Furthermore, the pulsation of Cepheids relies on the star's self-gravitation, therefore, unusual gravitational behaviour could lead to a modification of their period–luminosity relation. However there are currently no signs of anomalous behaviour in the data (Jain, Vikram & Sakstein 2012).

3.2 Baryon acoustic oscillations

Encoded within the distribution of galaxies is a useful comoving ruler, a modest excess of galaxy pairs at $\sim$150 Mpc, relating to the distance sound waves were able to propagate prior to recombination. In Fourier space this feature is referred to as the BAO. For a given BAO observation, the relevant cosmological information can often be distilled to a single data point, that of $D_{\mathrm{V}}(z)/r_{\mathrm{s}}$, where r_{s} is the sound horizon at the baryon drag epoch, and the volume element $D_{\mathrm{V}}(z)$ is defined in terms of the angular diameter distance $D_{\mathrm{A}}(z)$ and Hubble parameter $H(z)$:

$$D_{\mathrm{V}}(z) \equiv \left[(1+z)^2 D_{\mathrm{A}}^2(z)\frac{cz}{H(z)}\right]^{1/3}. \tag{10}$$

The most conservative treatment of BAO data would be to treat r_{s} as an unknown quantity, and eliminate it by taking the ratio of $D_{\mathrm{V}}(z)$ at two separate redshifts. However since the CMB provides us with a good understanding of the conditions in the early Universe, we have the opportunity to determine r_{s} for a given set of cosmological parameters. For our purposes this quantity is derived using equation (6) from Eisenstein & Hu (1998).

Where stated, we utilize measurements of $D_{\mathrm{V}}(z)/r_{\mathrm{s}}$ at two different redshifts. Anderson et al. (2012) present BAO constraints from the Baryon Oscillation Spectroscopic Survey (BOSS), and we also include a measurement from the Sloan Digital Sky Survey (SDSS) luminous red galaxies (Padmanabhan et al. 2012). Both studies present results before and after a reconstruction method has been applied, a technique which increases the prominence of the BAO by partially reversing the effects of gravitational infall. We conservatively adopt the BAO results prior to reconstruction, since we wish to avoid making assumptions relating to the growth of density perturbations. The change in our results is negligible, however, when the reconstructed values are included. For the BOSS CMASS sample, the 'consensus' result (Anderson et al. 2012) averages the power spectrum and correlation function analyses, giving $D_{\mathrm{V}}/r_{\mathrm{s}}(z = 0.57) = 13.67 \pm 0.22$. The SDSS data point is given by $D_{\mathrm{V}}/r_{\mathrm{s}}(z = 0.35) = 8.89 \pm 0.31$. We neglect any covariance in the two data points generated by the small overlap between the SDSS and BOSS volumes, which spans less than 9 per cent of the BOSS volume (Anderson et al. 2012).

It should be noted that when combined with *Wilkinson Microwave Anisotropy Probe* 7-year (*WMAP*7) data, recent BAO results suggest values of H_0 which are in mild tension with the measurement from Riess et al. (2011). For example Anderson et al. (2012) find $H_0 = 68.4 \pm 1.3\,\mathrm{km\,s^{-1}\,Mpc^{-1}}$, while studies from 6dFGS and SDSS measure 67 ± 3.2 and $69.8 \pm 1.2\,\mathrm{km\,s^{-1}\,Mpc^{-1}}$, respectively (Beutler et al. 2011; Mehta et al. 2012). We present separate results generated using the H_0 and BAO data in Section 6.

3.3 Cosmic microwave background ($\ell > 100$)

We utilize the temperature C_ℓ^{TT} and polarization C_ℓ^{TE} spectra from the *WMAP*7 data (Larson et al. 2011). This serves two purposes, first it offers strong constraints on a number of cosmological parameters, but it also serves to directly assist in the measurement of the growth of structure. Our current position in space and time, $z = 0$, acts as the benchmark from which all cosmological distance measurements are made. However when mapping the growth of structure, it is the epoch of recombination at $z \simeq 1100$ which effectively acts as our starting point. The CMB provides a precise measure of the amplitude of density fluctuations in the early Universe. Combining this with a measure of the clustering amplitude at low redshift provides a strong lever for constraining the growth rate between these two epochs.

Large angular scales of the CMB are sensitive to modified gravity models, and these are treated separately in Section 4.3. The implications for modified gravity have already been studied (see for example Zuntz et al. 2012), and here our primary focus is to explore the constraints available from lensing. For the range of values considered in this study, μ_0 and Σ_0 were found to impose negligible change in either C_ℓ^{TT} or C_ℓ^{TE} beyond the $\ell = 100$ multipole (see Section 4.3). Unless otherwise stated we simply truncate the largest angular scales, such that only $\ell \geq 100$ are included in our analysis. In doing so we negate the impact of the ISW, and utilize *WMAP7* only to assist in measuring the conventional cosmological parameters. For further details of our treatment of the CMB, see Appendix A.

4 GRAVITATIONAL DATA

4.1 Cosmic shear

Gravitational lensing by large-scale structures in the Universe coherently distorts the observed shapes of distant galaxies. This cosmic shear distortion can be used to directly probe dark matter, and, when analysed in tomographic redshift bins, can also reveal the growth of structure. It also acts as a useful tool for testing the laws of gravity (White & Kochanek 2001; Doré et al. 2007). We use tomographic cosmic shear data from CFHTLenS, published in Benjamin et al. (2012). CFHTLenS is a 154 deg^2 deep multicolour survey optimized for weak lensing analyses, where the data were obtained as part of the CFHT Legacy Survey on the 3.6-m CFHT. Weak gravitational lensing is widely recognized as one of the most powerful probes of cosmology, but also one of the most technically challenging, as the weak cosmic shear distortion must be separated from other sources of image distortion induced by the atmosphere, telescope and detector. The CFHTLenS analysis represents the current state-of-the-art in weak lensing data processing (Erben et al. 2009), weak lensing measurement (Miller et al. 2013), photometric redshift measurement (Hildebrandt et al. 2012) and systematic error analysis (Heymans et al. 2012). Benjamin et al. (2012) also use an angular cross-correlation analysis to verify the accuracy of the

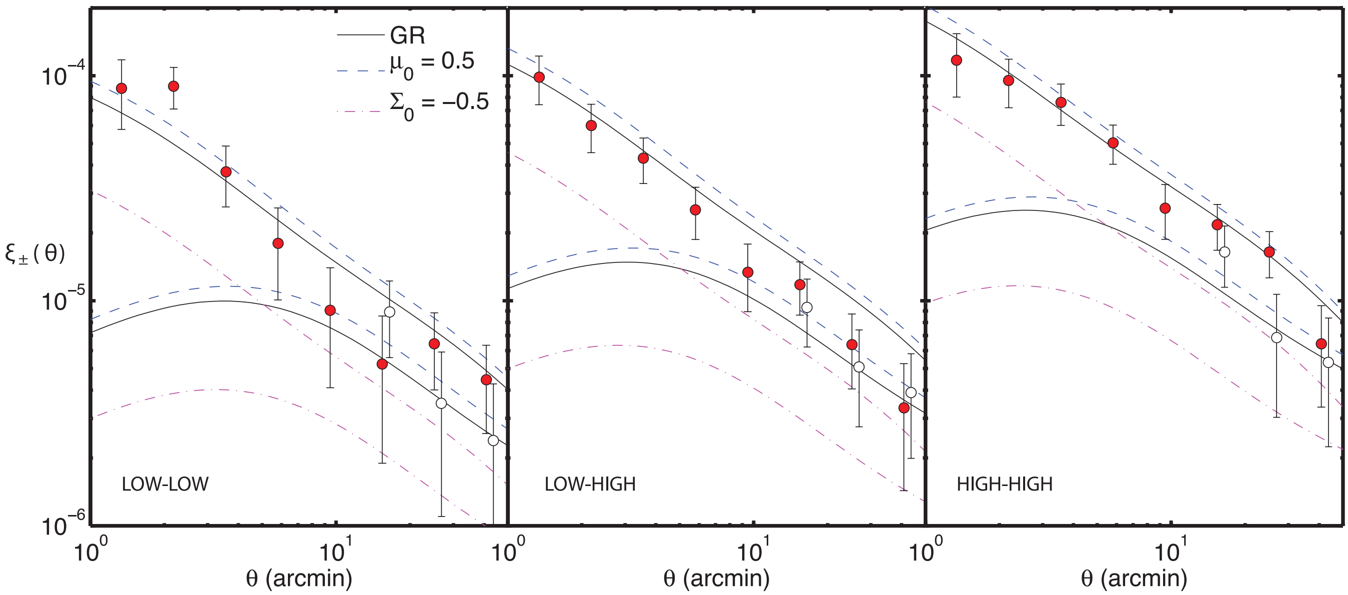

Figure 2. The cosmic shear data from CFHTLenS. Each panel contains the two lensing correlation functions, $\xi_+(\theta)$ (filled) and $\xi_-(\theta)$ (empty) with the $\xi_-(\theta)$ points slightly offset for clarity. The source galaxies are divided into two redshift bins, a 'low'-redshift bin with $0.5 < z \le 0.85$ and a 'high'-redshift bin with $0.85 < z \le 1.3$. The left-, middle and right-hand panels display data from the low–low, low–high and high–high correlations. In each case, the black lines are the set of theoretical curves corresponding to $\xi_+(\theta)$ (upper) and $\xi_-(\theta)$ (lower) for the best-fitting ΛCDM cosmology. The dashed lines correspond to a cosmological model with the same expansion history $H(z)$ as the best-fitting model, but with a boost in the effective gravitational constant ($\mu_0 = 0.5$; $\Sigma_0 = 0$). The dot–dashed lines demonstrate the signal one expects if the present-day ($z = 0$) gravitational potentials are associated with Newtonian gravity ($\mu_0 = 0$; $\Sigma_0 = -0.5$).

measured redshift distributions that we use in this analysis. These results, in combination with the cosmology insensitive joint shear–redshift systematic test presented in Heymans et al. (2012), allow us to conclude that the analysis of the survey data is robust within our uncertainties and residual systematics levels and can therefore be used to test the laws of gravity.

Benjamin et al. (2012) analyse two high-redshift bins with $0.5 < z \le 0.85$ and $0.85 < z \le 1.3$, presenting the autocorrelation and cross-correlations of the angular two-point shear correlation functions $\xi_\pm^{ij}(\theta)$ over scales $1 < \theta < 40$ arcmin, as shown in Fig. 2. The choice to use only two broad high-redshift bins in this tomographic analysis was motivated by the desire to mitigate the impact of intrinsic galaxy alignments on the tomographic measurements (see for example Heymans et al. 2006; Joachimi et al. 2011, and references therein). For this combination of high-redshift bins, the contamination to the signal is expected to be at the per cent level and so we follow Benjamin et al. (2012) by neglecting this source of error in our analysis. We use a covariance matrix between the resulting correlated data points as estimated from *N*-body lensing simulations (Harnois-Déraps, Vafaei & Van Waerbeke 2012), discussed and verified in Kilbinger et al. (2012) and Benjamin et al. (2012).

Theoretical predictions for these correlation functions are generated using the relation

$$\xi_\pm^{i,j}(\theta) = \frac{1}{2\pi}\int_0^\infty P_\kappa^{i,j}(\ell)\, J_{0/4}(\ell\theta)\, \ell\, \mathrm{d}\ell, \tag{11}$$

where $P_\kappa^{i,j}(\ell)$ is given in equation (8) and $J_{0/4}$ are the zeroth- and fourth-order Bessel functions.

On the smallest angular scales studied by cosmic shear it is likely that baryonic physics will disturb the density perturbations (Semboloni et al. 2011). This is also the regime where our prescription for modelling the non-linear correction to the matter power spectrum (see below) begins to break down. Because of the very different nature of the zeroth and fourth Bessel functions, the $\xi_-(\theta)$ correlation function is sensitive to considerably smaller scales than $\xi_+(\theta)$ for a given θ value. For the ξ_- statistic we therefore only include the larger angular scales $\theta > 10$ arcmin. These data points are presented in Fig. 2, alongside theoretical predictions from the best-fitting ΛCDM cosmology and two illustrative modified gravity scenarios. From left to right, the three panels in Fig. 2 relate to the correlations of the low–low, low–high and high–high redshift bins. A more detailed justification for the angular cuts and their implications are discussed in Benjamin et al. (2012); in any case we find no significant change in our results when the small angular scales of $\xi_-(\theta)$ are included due to the high correlation between the points and their relatively low signal-to-noise ratio. We further investigate the impact of truncating smaller length scales in Kitching et al. (in preparation).

4.2 Redshift-space distortions

Doppler distortions of the galaxy clustering pattern provide an independent probe of gravitational physics, by revealing the coherent flows of galaxies which trace the growth of cosmic structure. The principal effect on large scales is an amplification of apparent galaxy clustering along the line-of-sight, breaking the statistical isotropy. This anisotropy can be extracted from the two-point clustering statistics of a galaxy redshift survey, yielding a measurement of $f(z)\sigma_8(z)$. Here f is the growth rate of structure, expressible in terms of the growth factor $D(a)$ as $f \equiv \mathrm{d}\ln D/\mathrm{d}\ln a$, where the growth factor describes the evolution of the amplitude of a single linear density perturbation $\delta(a) = D(a)\delta(1)$. The function $\sigma_8(z)$ quantifies the amplitude of the linear clustering of matter at a given redshift, and is defined as the rms density variation in spheres of comoving radius 8 h^{-1} Mpc. The degeneracy between f and σ_8 arises due to the unknown galaxy bias factor b: the observables are the anisotropy in the galaxy clustering pattern which depends on $\beta \equiv f/b$, and the galaxy clustering amplitude which depends on $b\sigma_8(z)$.

Measurements of RSDs from a galaxy redshift survey are degenerate with a second isotropy-breaking mechanism: the Alcock–Paczynski distortion (Alcock & Paczynski 1979), which arises if the fiducial cosmological model we adopt for converting redshifts and angles to physical distances differs from the true cosmological model (Ballinger, Peacock & Heavens 1996; Matsubara & Suto 1996; Seo & Eisenstein 2003; Simpson & Peacock 2010). The amplitude of Alcock–Paczynski anisotropy depends on the quantity

$$F(z) = (1+z)D_{\mathrm{A}}(z)H(z)/c, \tag{12}$$

in terms of the angular diameter distance $D_A(z)$ and Hubble expansion parameter $H(z)$. Although measurements of F and $f\sigma_8$ from a galaxy redshift survey are strongly correlated, the angular distortions imprinted in the clustering pattern by these two effects are sufficiently different that the degeneracy can be broken.

The measurements of $(f\sigma_8, F)$ that we use in this study are derived from the WiggleZ published in Blake et al. (2012) and from 6dFGS, as presented in Beutler et al. (2012). Fig. 3 compares the measurements of $f\sigma_8$ from WiggleZ (squares) and the 6dFGS (diamond) to the best-fitting ΛCDM cosmology and two examples modified gravity scenarios with $\mu_0 = 0.5$ and 1.0 (dashed).

The WiggleZ (Drinkwater et al. 2010) at the 3.9-m Anglo-Australian Telescope has mapped a cosmic volume ∼1 Gpc^3 over the redshift range $0 < z < 1$. By covering a total of ∼800 deg^2 of sky the WiggleZ mapped about 100 times more effective cosmic volume in the $z > 0.5$ Universe than previous galaxy redshift surveys. Target galaxies were chosen by a joint selection in ultraviolet (UV) and optical wavebands, using observations by the *Galaxy Evolution Explorer* (*GALEX*) satellite (Martin et al. 2005) matched with ground-based optical imaging from the SDSS (York et al. 2000) in the Northern Galactic Cap, and from the Red Sequence Cluster Survey 2 (RCS2; Gilbank et al. 2011) in the Southern Galactic Cap. A series of magnitude and colour cuts (Drinkwater et al. 2010) was used to preferentially select high-redshift star-forming galaxies with

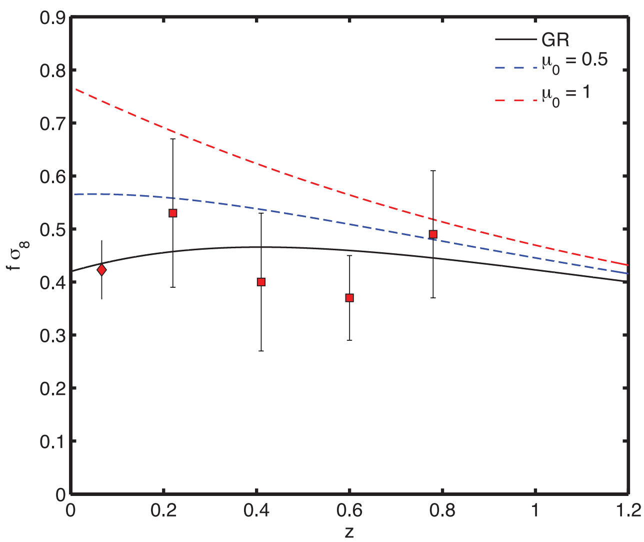

Figure 3. The growth data from WiggleZ (Blake et al. 2012) and 6dFGS (Beutler et al. 2012). The black line is the corresponding theoretical curve for the best-fitting ΛCDM cosmology. The dashed lines correspond to the same cosmology but with a boost in effective gravitational constant μ_0.

bright emission lines that were then observed using the AAOmega multiobject spectrograph (Sharp et al. 2006) in 1-h exposures.

The 6dFGS is a near-infrared selected combined redshift and peculiar velocity survey covering nearly the entire southern sky with Galactic latitude $|b| < 10°$. It was undertaken with the Six-degree Field (6dF) multifibre instrument on the UK Schmidt Telescope from 2001 to 2006 (Jones et al. 2004, 2009). The redshift survey covers 125 000 galaxies with $8.75 \le K \le 12.75$ and median redshift $z = 0.052$.

In this study we use the WiggleZ joint measurements of $(f\sigma_8, F)$ in three different redshift slices with effective redshifts $z = 0.44$, 0.60 and 0.73. The marginalized measurements of the growth rate in these redshift slices are $f\sigma_8(z) = (0.41 \pm 0.08, 0.39 \pm 0.06, 0.44 \pm 0.07)$. The marginalized measurements of the Alcock–Paczynski distortion parameter are $F = (0.48 \pm 0.05, 0.65 \pm 0.05, 0.86 \pm 0.07)$. The correlation coefficients between these pairs of values are (0.73, 0.74, 0.85). These measurements were derived by fitting the non-linear clustering model provided by Jennings, Baugh & Pascoli (2011) to the 2D WiggleZ power spectrum over the range of wavenumbers $0 < k < 0.2\,h$ Mpc^{-1}, marginalizing over the linear galaxy bias factor and a small-scale velocity dispersion σ_v. Blake et al. (2011) carried out a suite of systematics tests to demonstrate that the derived results did not depend on either the fitting range or the non-linear model of RSDs adopted; we refer the reader to this paper for further details. There is some overlap (∼500 deg^2) between the sky areas surveyed by WiggleZ and the SDSS/BOSS surveys that are used in our results which are stated to include BAO. However, based on the nature of the geometric BAO data being very different to that used for the RSD gravitational measurements we assume that any covariance in these derived results is negligible. In essence, when considering the redshift-space galaxy power spectrum, the location of the acoustic peak bears little connection to the power of the quadrupole.

We also include the single data point $f\sigma_8(z = 0.067) = 0.423 \pm 0.055$ (Beutler et al. 2012) from the 6dFGS. Because of its low redshift, this result benefits from having negligible sensitivity to the Alcock–Paczynski distortion, and a large sensitivity to our modified gravity parameter μ_0, as can be seen in Fig. 3. The 6dFGS measurement was derived using the non-linear model of Jennings et al. (2011), including wide-angle corrections, fit to the 2D galaxy redshift-space correlation function for transverse separations $r_{\mathrm{p}} > 16\,h^{-1}$ Mpc. The growth-rate measurements obtained, marginalized over bias, were consistent with fitting an empirical streaming model to the results (see Beutler et al. 2012, for further details). While the WiggleZ and 6dFGS analyses differ in their utilization of the power spectrum and correlation function, respectively, their approach to modelling non-linear corrections and galaxy bias remains consistent.

4.3 Cosmic microwave background ($\ell < 100$)

When in the presence of a time-dependent gravitational potential, a particle may extract or lose energy from its surroundings. It is this mechanism which space probes exploit when passing close to planets for a gravitational slingshot. For CMB photons, the gravitational source is associated with large-scale density perturbations. In GR, if the photon passes through a high-density region of the Universe, the dark-energy-induced decay of the gravitational potentials $\Phi(x, t)$ and $\Psi(x, t)$ results in a net energy gain, with a blueshifting effect. Conversely, passing through a void result in a net loss of energy.

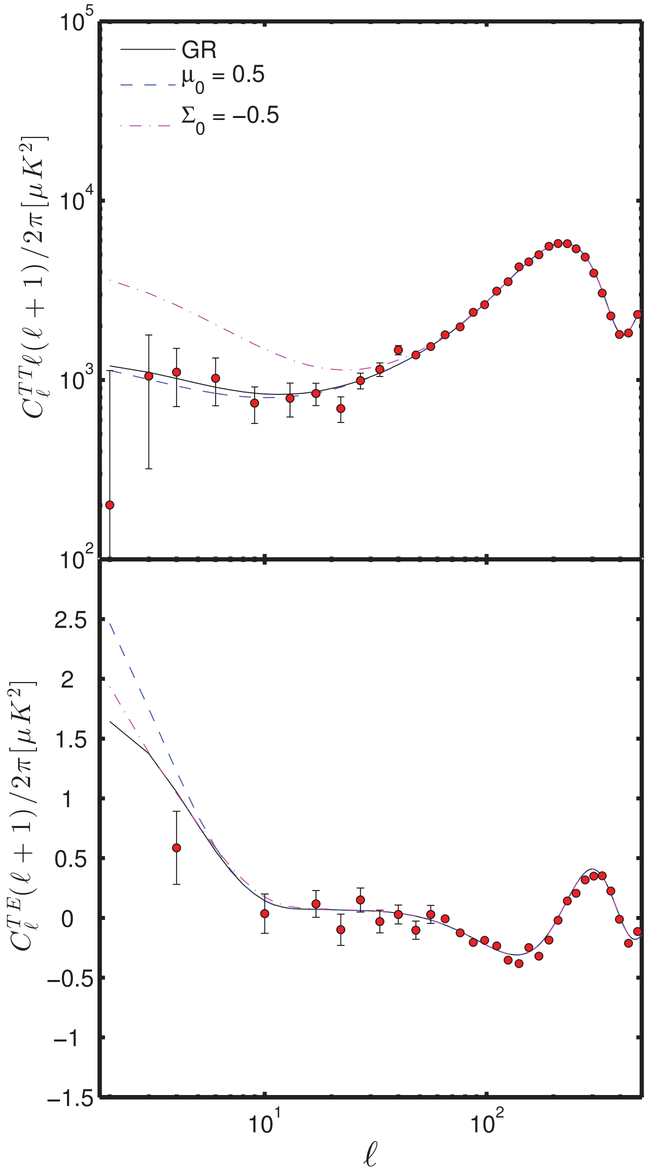

Figure 4. Modifications to the temperature (upper panel) and temperature–polarization (lower panel) power spectra of the CMB. In each panel the black line is the corresponding theory curves for the best-fitting ΛCDM cosmology. The dashed and dash–dot lines represent the same modifications to our modified gravity parameters as seen in Fig. 2. Superposed on these theoretical predictions are the binned data points from the *WMAP*7 observations (Larson et al. 2011).

The resulting temperature perturbation may be expressed by the line integral:

$$\frac{\Delta T}{T} = -\int \frac{\mathrm{d}}{\mathrm{d}\eta}\left[\Phi(x,t) + \Psi(x,t)\right]\mathrm{d}\eta, \tag{13}$$

where η is the conformal time defined by $\mathrm{d}\eta \equiv \mathrm{d}t/a$, and the integral follows the path of the photon. We can see from equation (13) that this ISW effect is another probe which, like gravitational lensing, retains sensitivity to both gravitational potentials. However the ISW signal within the temperature anisotropies is only expected to be significant on large angular scales, $\ell < 100$ as illustrated by Fig. 4 which compares the temperature (upper) and temperature–polarization (lower panel) GR power spectra of the CMB (solid) with data points used in this analysis, from the *WMAP*7 observations (Larson et al. 2011). The dashed and dash–dot lines represent the same modifications to our modified gravity parameters as seen in Fig. 2 with $\mu_0 = 0.5, \Sigma_0 = 0$ (dashed) and $\mu_0 = 0, \Sigma_0 = -0.5$ (dot–dashed). These modified gravity models of the CMB power spectrum deviate from GR only on the largest angular scales. Observational ISW studies are therefore heavily restricted by cosmic variance, and future experiments cannot be expected to improve upon *WMAP*, unless we begin to include cross-correlations with large-scale structure. Note that throughout this work, we use the term ISW to refer to the phenomenon which arises in the CMB power spectrum, not the cross-correlation between the CMB and the distribution of galaxies.

For any metric theory of gravity, density fluctuations on scales beyond the horizon are subject to a stringent consistency relation. Since material cannot be transported at superluminal velocities, superhorizon perturbations are destined to evolve along a path determined by the global expansion (Bertschinger 2006). Therefore the constraints presented which incorporate the ISW should be treated with this in mind, as the ISW involves scales very much larger than those studied by gravitational lensing, a regime where there is a stronger expectation that the values of μ_0 and Σ_0 are close to zero.

5 METHODS

Using a combination of geometric data (presented in Section 3) and gravitational data (presented in Section 4), we use a maximum likelihood analysis to constrain our phenomenological modified gravity parameters μ_0 and Σ_0.

To generate the likelihood values we modified CosmoPMC (Kilbinger et al. 2011), an adaptive importance sampling code, to incorporate the alterations to the growth of structure (equation 7) and cosmic shear signal (equation 8). A customized version of MGCAMB (Lewis, Challinor & Lasenby 2000; Hojjati, Pogosian & Zhao 2011) was used to evaluate the CMB anisotropies for a given set of cosmological parameters, which are then assessed with the *WMAP* likelihood code.[1] Our analysis spans the parameter set $\{\Omega_\mathrm{m}, \Omega_\mathrm{b}, h, \tau, n_\mathrm{s}, A_\mathrm{SZ}, \Delta_R^2, \mu_0, \Sigma_0\}$, where τ is the optical depth, n_s the spectral index, A_SZ the amplitude of the Sunyaev–Zel'dovich template for the CMB (Komatsu & Seljak 2002; Spergel et al. 2007) and Δ_R^2 controls the primordial amplitude of matter perturbations. Where specified we also marginalize over a time-independent effective equation of state for dark energy w and global curvature Ω_K, in addition to the aforementioned set of parameters. We adopt flat priors throughout, spanning the following parameter ranges: $\Omega_\mathrm{m} \in [0.05; 1]$, $\Omega_\mathrm{b} \in [0.01; 0.1]$, $h \in [0.5; 1]$, $\tau \in [0.02; 0.3]$, $n_\mathrm{s} \in [0.8; 1.2]$, $A_\mathrm{SZ} \in [0; 2]$, $\Delta_R^2 \in [1.8; 3.5] \times 10^{-9}$, $\mu_0 \in [-4.0; 4.0]$, $\Sigma_0 \in [-4.0; 4.0]$, $w \in [-1.5; -0.3]$ and $\Omega_K \in [-0.1; 0.1]$. In most cases these boundaries extend well beyond the regions of high likelihood, except for A_SZ which is not well constrained, however, its impact on the other parameters is negligible. In order to generate visualizations of the generated samples we make use of code adapted from COSMOLOGUI.[2]

In generating the matter power spectrum, the CosmoPMC package makes use of the Eisenstein & Hu (1998) transfer function. The growth factor is determined in accordance with the modified equation (7), before adding a non-linear correction using the prescription of Smith et al. (2003). To compensate for cosmologies where $w \neq -1$, a further modulation of the non-linear power is required, as

[1] http://lambda.gsfc.nasa.gov

[2] http://www.sarahbridle.net/cosmologui

presented in McDonald, Trac & Contaldi (2006). We make use of the scaling correction provided in Schrabback et al. (2010) to apply this formalism across our full range of parameter space. However it should be noted that our results only have a weak dependence on this correction. The mean values of μ_0, Σ_0 and w all change by less than 0.02 when the prescription from Schrabback et al. (2010) is omitted, which is well within our statistical errors. The value of the Σ_0 parameter has no impact on structure formation, and while we may expect non-zero values of μ_0 to alter the non-linear correction to the matter power spectrum, we do not attempt to correct it here. We expect the prescription of Smith et al. (2003) to remain a reasonably good approximation in the presence of a simple scale-independent modification to the growth of structure such as that induced by μ_0. To first order the correction associated with non-linear power is simply a function of the ambient linear power at that epoch; how quickly it arrives at this state is of less importance. In any case, modified behaviour on non-linear scales would still weaken the fit to the data achievable within the framework of GR.

6 RESULTS

6.1 ΛCDM

We begin with the simple case of a flat ΛCDM geometry. In this scenario we are making a strong assumption about the form of the cosmic expansion history $H(z)$, but in doing so make significant gains in the precision of our likelihood contours. Any apparent deviation from GR witnessed at this stage must be interpreted with caution due to the strong assumptions of this relatively simple model.

The left-hand panel of Fig. 5 illustrates the variety of 1 and 2σ confidence intervals for different combinations of data sets. Each of these contours include the auxiliary data of *WMAP*7 ($\ell \geq 100$) and a prior on H_0. The horizontal (green) contours reflect the pure μ_0 measurement established with the WiggleZ data. The Σ_0 parameter is unconstrained since the peculiar motions of galaxies are slow ($v \ll c$), and are therefore insensitive to the spatial curvature $\Phi(x, t)$. The near-vertical (red) contours correspond to the cosmic shear data from CFHTLenS. Unsurprisingly, this is predominantly a measure of Σ_0 due to its direct influence on the lensing potential. The mild sensitivity to μ_0 arises from the amplitude of the matter power spectrum entering in equation (8). A positive value of μ_0 enhances the growth of structure and thus strengthens the cosmic shear signal (for a given primordial amplitude). This can be offset with a negative value of Σ_0, weakening the deflection of light and leading to the negatively sloped degeneracy direction seen in the red contours of Fig. 5. When combined (blue), the near-orthogonal degeneracy directions of WiggleZ and CFHTLenS produce a considerable reduction in the permitted area of parameter space. The tightest constraints (white) emerge from adding in BAO from BOSS and the ISW large-scale anisotropies ($\ell < 100$) from *WMAP*7. None of these combinations shows any preference for non-zero values of either μ_0 or Σ_0, suggesting that GR remains a successful model of gravitation on cosmological scales, for both relativistic and non-relativistic particles.

The mean and 1σ errors in the modified gravity parameters are found to be $\mu_0 = 0.05 \pm 0.25$ and $\Sigma_0 = 0.00 \pm 0.14$. The results for other combinations of data sets can be found in Table 1.

How sensitive are we to the choice of auxiliary data? The right-hand panel of Fig. 5 contains the same data sets and layout as the left-hand panel, except here we have replaced the prior on H_0 with the BAO data summarized in Section 3.2. The BAO prefer a higher value of Ω_m (or equivalently, a lower value of H_0), and this does

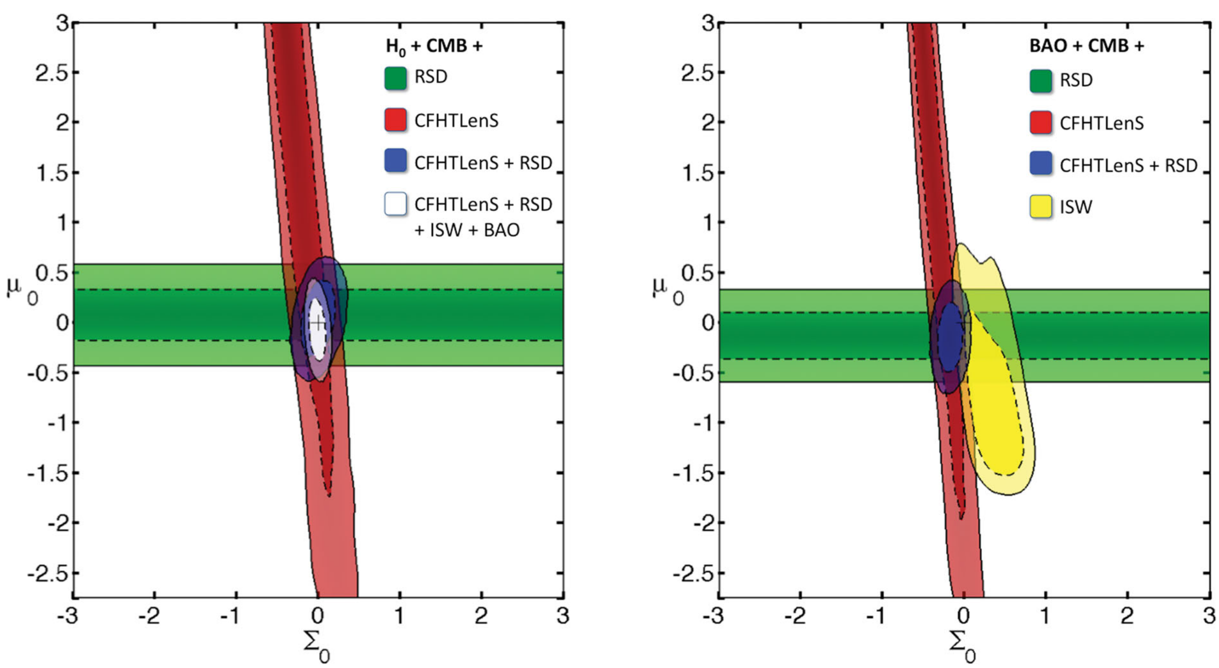

Figure 5. Left: constraints on the modified gravity parameters in a flat ΛCDM background from RSDs (green), weak lensing (red) and combined (blue). (68 and 95 per cent CL). The dashed and solid contours represent the 68 and 95 per cent confidence intervals, respectively. Two auxiliary data sets are used here to break degeneracies with the conventional cosmological parameters. These are the small-angle anisotropies from *WMAP*7 ($\ell \geq 100$), and a prior on H_0 from (Riess et al. 2011). The cross positioned at the origin denotes the prediction of GR. Right: the red, green and blue contours are the same as the left-hand panel, except the prior on H_0 has been replaced by measurements of the BAO as detailed in Section 3.2. The yellow contours signify the constraints derived from the full *WMAP*7 power spectra, including the large angular scales ($\ell < 100$). The white contours in the left-hand panel show the constraints when all data sets are analysed in combination.

Table 1. Parameter constraints for different combinations of data set and parameter space. The three different backgrounds we explore are flat ΛCDM, flat wCDM and the non-flat wCDM which we denote as owCDM. All constraints make use of the small-scale anisotropies from *WMAP7* ($\ell \geq 100$), while those marked ISW also utilize the larger angular scales.

Background	Data (+ CMB + H_0)	μ_0	Σ_0	Ω_m	H_0	σ_8	w	Ω_K
ΛCDM	CFHTLenS	1.2 ± 2.2	-0.17 ± 0.28	0.260 ± 0.024	71.3 ± 2.3	0.96 ± 0.24	⋯	⋯
ΛCDM	RSD	0.08 ± 0.25	⋯	0.254 ± 0.023	71.8 ± 2.2	0.801 ± 0.024	⋯	⋯
ΛCDM	CFHTLenS + RSD	0.05 ± 0.25	0.00 ± 0.14	0.256 ± 0.023	71.6 ± 2.2	0.804 ± 0.023	⋯	⋯
wCDM	CFHTLenS + RSD + BAO	-0.59 ± 0.34	-0.19 ± 0.11	0.272 ± 0.015	71.7 ± 1.8	0.820 ± 0.025	-1.19 ± 0.10	⋯
owCDM	CFHTLenS + RSD + BAO	-0.65 ± 0.34	-0.26 ± 0.12	0.289 ± 0.021	71.6 ± 1.8	0.833 ± 0.028	-1.16 ± 0.10	0.0096 ± 0.0087
Background	Data (+ CMB + BAO)	μ_0	Σ_0	Ω_m	H_0	σ_8	w	Ω_K
ΛCDM	CFHTLenS	1.0 ± 2.2	-0.31 ± 0.24	0.305 ± 0.018	67.2 ± 1.4	0.95 ± 0.24	⋯	⋯
ΛCDM	RSD	-0.13 ± 0.23	⋯	0.300 ± 0.017	67.5 ± 1.4	0.807 ± 0.023	⋯	⋯
ΛCDM	ISW	-0.62 ± 0.64	0.34 ± 0.22	0.294 ± 0.015	68.2 ± 1.2	0.768 ± 0.068	⋯	⋯
ΛCDM	CFHTLenS + RSD	-0.12 ± 0.23	-0.17 ± 0.10	0.300 ± 0.017	67.6 ± 1.4	0.807 ± 0.023	⋯	⋯
ΛCDM	CFHTLenS + RSD + ISW + H_0	-0.06 ± 0.21	-0.010 ± 0.068	0.273 ± 0.010	70.10 ± 0.97	0.803 ± 0.022	⋯	⋯

push the lensing data to predict a lower value of σ_8, which pushes the bulk of the likelihood towards negative values for Σ_0. This results in constraints of $\mu_0 = -0.12 \pm 0.23$ and $\Sigma_0 = -0.17 \pm 0.10$. The combination of CFHTLenS and RSD data (blue) can be compared with the constraints derived from the full *WMAP7* power spectra, including the ISW, and BAO (yellow).

6.2 *w*CDM

The dangers of confusing the signatures of modified geometry and modified gravity have previously been highlighted in the literature (see e.g. Simpson & Peacock 2010). In order to claim that we are testing GR and not simply ΛCDM we must therefore allow greater freedom in the cosmic expansion history $H(z)$. This is inevitably accompanied by some loss of precision, so we shall restrict ourselves to adding one extra parameter. In Fig. 6 we utilize both H_0 and BAO, in combination with CFHTLenS, RSD and the small angular scales of *WMAP7*, conservatively omitting the ISW information for the reasons outlined in Section 4.3. While the green contour in the left-hand panel corresponds to the standard flat ΛCDM background, the blue contours presented in the left-hand and centre panels allow the effective dark energy equation of state w to deviate from -1. The centre panel illustrates a degeneracy which causes the confidence contours to broaden. More positive values of w lead to a greater prevalence of dark energy at higher redshift (for a given value of Ω_m) and thus a slowing of the growth of structure. This can be compensated by enhancing the value of μ, which accelerates the growth of structure, leading to a similar growth history $f(z)$ to GR. For a wCDM cosmology the mean and 68 per cent confidence intervals are given by $\mu_0 = -0.59 \pm 0.34$, $\Sigma_0 = -0.19 \pm 0.11$ and $w = -1.19 \pm 0.1$. More detailed results are presented in Table 1.

6.3 o*w*CDM

We further generalize the expansion history by allowing for non-zero values of the global curvature Ω_k, using the same combination of data sets as in Section 6.2. The red contours in all three panels of Fig. 6 demonstrate the relatively small impact that non-flat geometries have on our confidence limits. The mean and 68 per cent confidence intervals are given by $\mu_0 = -0.65 \pm 0.34$, $\Sigma_0 = -0.26 \pm 0.12$, $\Omega_k = 0.096 \pm 0.087$ and $w = -1.16 \pm 0.10$.

7 ALTERNATIVE PARAMETRIZATIONS

In this section we consider the relationship between the (μ, Σ) parametrization adopted in this work, and three other popular parametrizations.

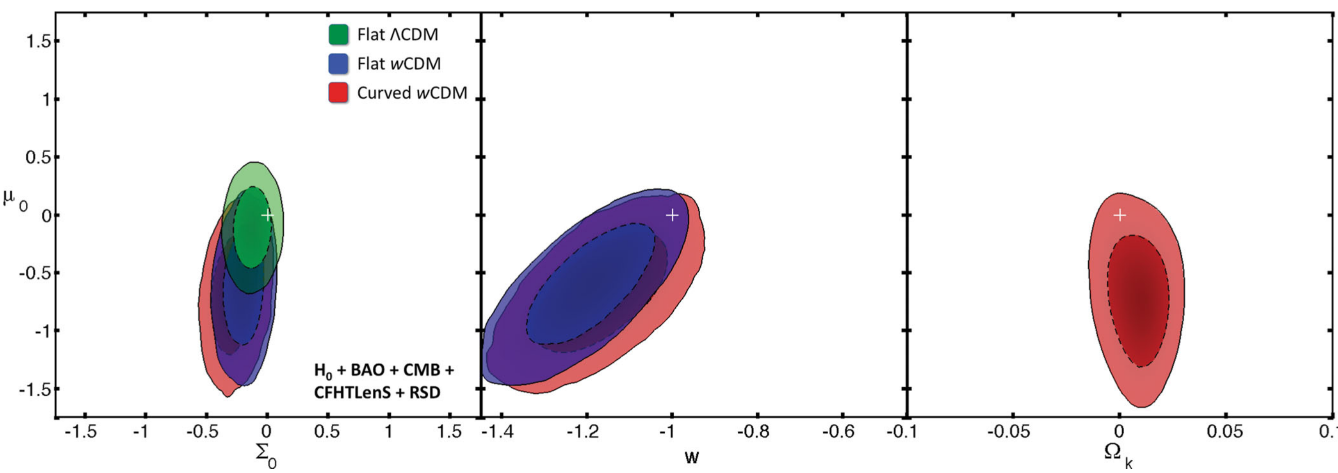

Figure 6. In this figure we extend our analysis to more general expansion histories. All of the above contours use a combination of cosmic shear and RSDs, combined with the geometric constraints from H_0, BAO and *WMAP7* ($\ell \geq 100$). The green set of contours in the left-hand panel corresponds to the background expansion of flat ΛCDM. For the blue contours in the left-hand and centre panels we allow the effective dark energy equation of state to deviate from $w = -1$, highlighting a significant degeneracy in the w–μ_0 plane. Finally, the red contours appearing in each of the panels allow non-zero curvature in addition to the wCDM background.

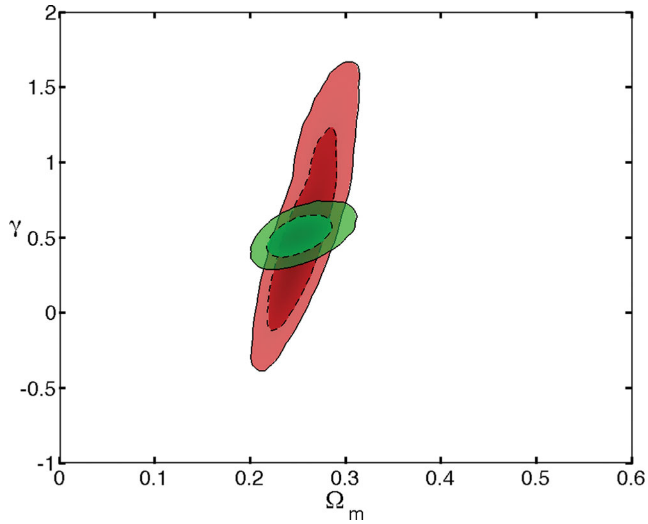

Figure 7. Confidence limits in the γ–Ω_m plane, as derived from RSDs (WiggleZ + 6dFGS) in green, and cosmic shear (CFHTLenS) in red (68 and 95 per cent CL), using small-angle anisotropies from *WMAP7* ($\ell \geq 100$), and a prior on H_0 as auxiliary data sets. Note that here γ is the only modified gravity parameter, as we have set $\Sigma(a) = 0$.

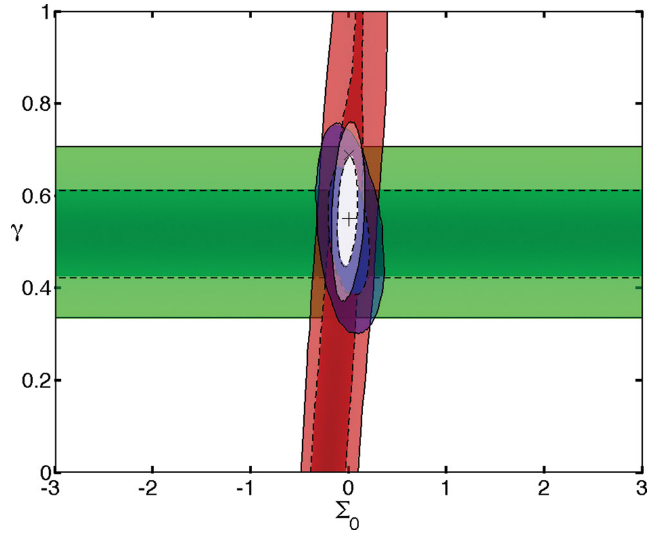

Figure 8. The same combinations of data as the left hand panel of Fig. 5, except we have replaced the μ_0 parameter with γ using the relation given by equation (16).

7.1 γ Parameter

A widely adopted parametrization for quantifying anomalous structure growth is the growth index γ (Wang & Steinhardt 1998; Linder 2005):

$$f(z) \simeq \Omega_m^{\gamma}(z), \tag{14}$$

where setting $\gamma = 0.55$ offers an estimate of the growth factors in wCDM cosmologies with sub-per cent accuracy. Equation (23) from Linder & Cahn (2007) gives us the relation

$$\gamma = \frac{3\left[1 - w - \frac{\mu(a)}{1-\Omega_m(a)}\right]}{5 - 6w} \tag{15}$$

for a constant equation of state w. In a flat ΛCDM Universe, this parameter may be expressed as a simple function of μ_0 and Ω_Λ,

$$\gamma = \frac{6}{11}\left[1 - \frac{\mu_0}{2\Omega_\Lambda}\right]. \tag{16}$$

Applying the prescription for the growth rate in equation (14) with a constant value the γ parameter does not offer a perfect reproduction of the growth of density perturbations in GR. This relationship provides a useful means to derive constraints in terms of γ without compromising the precision of the calculation. Constraints on this quantity are presented in the γ–Ω_m plane in Fig. 7. Gravitational lensing is not uniquely defined when using the γ parameter alone, so here we have simply set $\Sigma_0 = 0$ such that the lensing potential is unaltered from its conventional form. We find a value of $\gamma = 0.52 \pm 0.09$ for the case of a ΛCDM background. In Fig. 8, we then let Σ_0 vary, presenting constraints in the γ–Σ_0 plane.

7.2 E_G parameter

Proposed by Zhang et al. (2007), the E_G parameter encompasses contributions from both gravitational lensing and the motions of galaxies. This is in the form of a ratio which by construction nullifies contributions from both linear galaxy bias and the amplitude of the matter power spectrum. The result is a quantity which is sensitive to both the lensing potential and the rate of structure formation:

$$E_G \equiv \frac{\nabla^2(\Phi + \Psi)}{3H_0^2(1+z)\beta\delta}, \tag{17}$$

where $\beta \equiv f/b$. This technique has been applied to SDSS data in Reyes et al. (2010). We cannot directly measure E_G with the CFHTLenS and WiggleZ data sets, since they do not overlap in sky coverage. However, we can perform a direct mapping of the result from Reyes et al. (2010) on to the (μ, Σ) plane, utilizing the relationship

$$E_G \simeq \frac{\Omega_m\,[1 + \Sigma(\bar{z})]}{f(\bar{z})}, \tag{18}$$

where the dependence on μ arises through its influence on $f(\bar{z})$, the linear growth rate at the mean redshift of the survey. The results are presented in Fig. 9, where the red contours correspond to the confidence limits, in the μ_0–Σ_0 plane, arising from a combination of the measurement $E_G(z = 0.32) = 0.392 \pm 0.065$ (Reyes et al. 2010) with the BAO data from Section 3.2 which provide a constraint on Ω_m. The CMB does not provide further assistance in this case because the E_G parameter is insensitive to the amplitude of perturbations. For comparison, the inner blue contours match those in the right-hand panel of Fig. 5. We note that GR can readily generate departures from the conventional E_G value. For example in equation (18) the ratio $\Omega_m/f(\bar{z})$ changes when $\Omega_k \neq 0$ or $w \neq -1$. Similarly, radically different modified gravity models can generate an E_G value which appears consistent with the ΛCDM value. This is apparent from the degeneracy contour seen in Fig. 9, where large values of both μ and Σ enhance the growth rate and lensing signal, leaving their ratio in equation (17) unchanged.

7.3 Gravitational slip

Rather than modulating the sum of the two potentials using $\Sigma(a)$, it is often convenient to work in terms of the ratio of the potentials. One definition in this form is known as the gravitational slip ζ,

$$\zeta \equiv 1 - \frac{\Psi}{\Phi}, \tag{19}$$

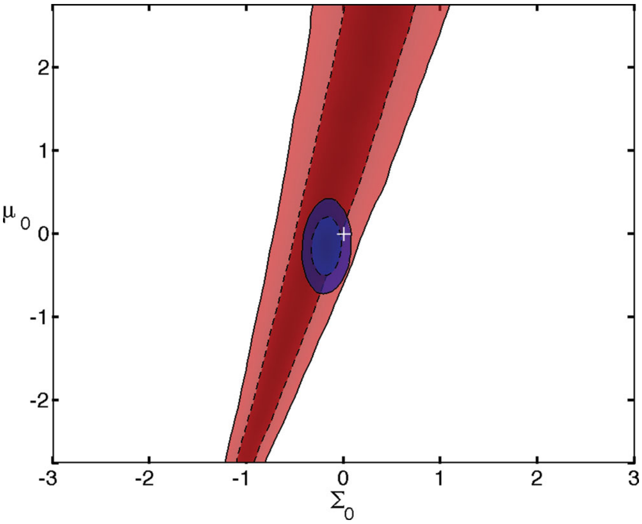

Figure 9. Confidence limits on the Σ_0 and μ_0 parameters derived from the measurement $E_G(z = 0.32) = 0.392 \pm 0.065$ (Reyes et al. 2010). The inner blue contours are the same as those in Fig. 5. Here we assume a ΛCDM cosmology.

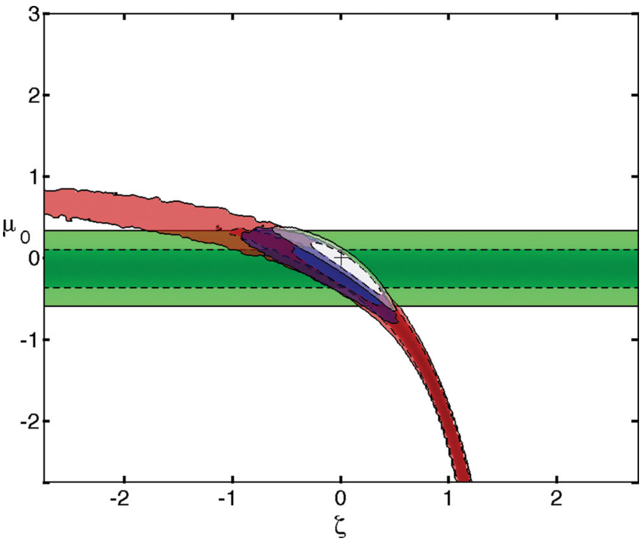

Figure 10. The same combinations of data as the left-hand panel of Fig. 5, except here we have replaced the Σ_0 parameter with the gravitational slip ζ_0 as defined in equation (19).

which we expect to be zero in GR, in the absence of anisotropic stress. This has been the focus of much theoretical exploration, for example Ferreira & Skordis (2010) demonstrate that for second-order theories we generally expect to find this value scales with the Newtonian potential and its time derivative.

Recasting ζ in terms of (μ, Σ) using equations (4) and (5):

$$\zeta(a) = \frac{2\,[\Sigma(a) - \mu(a)]}{1 + 2\Sigma(a) - \mu(a)}. \tag{20}$$

As an illustration in Fig. 10 we reformulate the x-axis from Fig. 5 in terms of ζ_0, the gravitational slip evaluated at $z = 0$. One striking feature of these contours are the long tails out to negative values of ζ and μ, corresponding to where the denominator Φ ventures close to zero. This suggests that the slip parameter may possess a pathological likelihood surface, and so for the purposes of performing Monte Carlo evaluations these contours are more safely generated as a derived parameter.

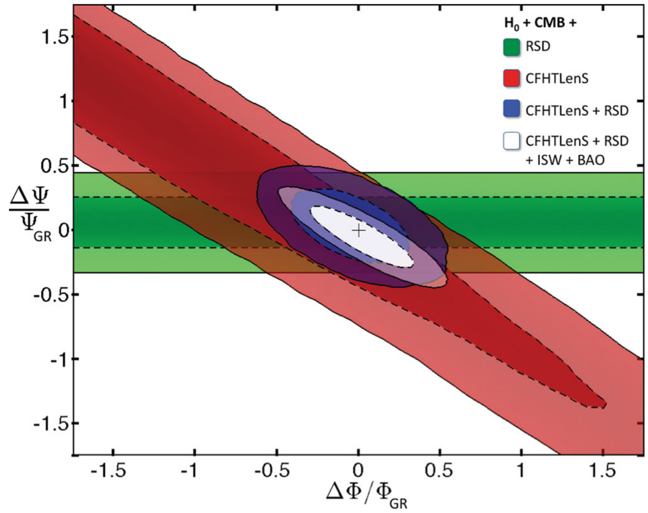

Figure 11. Here we explore fractional deviations in the two gravitational potentials, the Newtonian potential Ψ and the curvature potential Φ, from the GR value at $z = 0.5$. The prescription for this is given by equation (21). The contours represent the same combinations of data as those in the left-hand panel of Fig. 5.

7.4 Gravitational potentials

The RSD data, used in this analysis, exhibit a peak sensitivity to a modified gravity scenario at approximately $z \simeq 0.5$ (see Section 8). In Fig. 11 we therefore consider fractional deviations in the two gravitational potentials at this redshift, relative to their GR prediction for the same mass distribution. These are given by

$$\frac{\Delta\Psi}{\Psi} = \mu(z),$$
$$\frac{\Delta\Phi}{\Phi} = 2\Sigma(z) - \mu(z), \tag{21}$$

where $\Delta\Psi \equiv \Psi - \Psi_{GR}$. For our conservative combined lensing, RSD, H_0 and high ℓ *WMAP*7 data analysis we find cosmological deviations in the Newtonian potential and curvature potential from the prediction of GR to be $\Delta\Psi/\Psi = 0.05 \pm 0.25$ and $\Delta\Phi/\Phi = -0.05 \pm 0.3$, respectively [68 per cent confidence limits (CL)].

8 THEORETICAL MODELS

Below we briefly review some of the theoretical models which could generate a departure from $\mu_0 = \Sigma_0 = 0$, and interpret the implications of our results. There is such a plethora of modified gravity models, that no single choice of parametrization can adequately encompass all of them. This is a situation reminiscent of the dark energy equation of state, $w(z)$, except here we are faced with uncertainty not only in the functional form of the time dependence but also in its scale dependence. So how can we relate a given (μ, Σ) constraint to a specific model? The observed parameters $\hat{\mu}_0$ and $\hat{\Sigma}_0$ may be interpreted as a weighted integral over the true functional form $\mu(k, z)$, such that

$$\hat{\mu}_0 = \iint \phi(k, z)\, \mu(k, z) \frac{\Omega_\Lambda}{\Omega_\Lambda(z)}\, \mathrm{d}k\, \mathrm{d}z. \tag{22}$$

If we perform a scale- and time-dependent principal component analysis (see e.g. Zhao et al. 2009), then the weight function $\phi(k, z)$

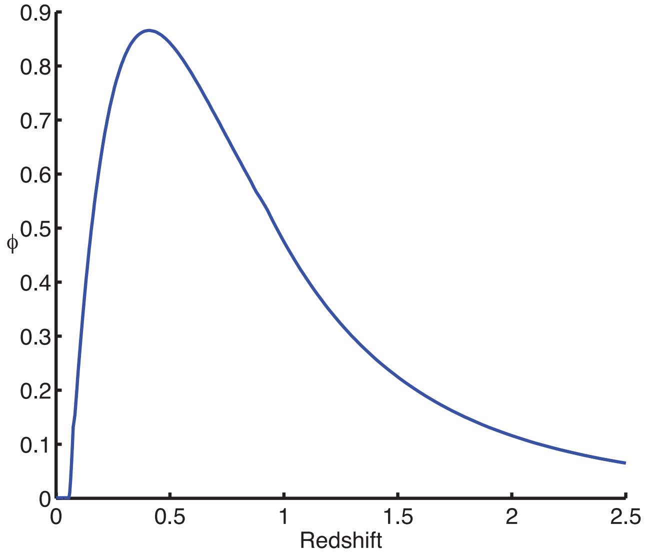

Figure 12. The redshift sensitivity of the modified gravity parameter μ_0. The weight function $\phi(z)$ is defined in equation (22) and evaluated with equation (23).

may be expressed in terms of the principal components $e_i(k, z)$ and the errors associated with their corresponding eigenvalues $\sigma(\alpha_j)$ (Simpson & Bridle 2006), such that

$$\phi(k, z) = \frac{\sum_i e_i(k, z) \iint e_i(k', z')\, \mathrm{d}k'\, \mathrm{d}z' / \sigma^2(\alpha_i)}{\sum_j \left[\iint e_j(k'', z'')\, \mathrm{d}k''\, \mathrm{d}z''\right]^2 / \sigma^2(\alpha_j)}. \tag{23}$$

The analysis of RSDs in Blake et al. (2012) includes information from the galaxy power spectrum up to a maximum wavenumber $k_{\max} = 0.2\,h\,\mathrm{Mpc}^{-1}$, corresponding to the regime over which the density and velocity fields are sufficiently linear for our theoretical models to remain valid. Since the number of Fourier modes increases towards higher k, the scale-dependent component of $\phi(k, z)$ peaks close to this value of $k_{\max}$, and $\phi(k, z) = 0$ for $k > k_{\max}$. We evaluate the redshift dependence of the weight function $\phi(z)$ associated with the combined WiggleZ and 6dFGS data of Fig. 3, following the prescription of Simpson & Bridle (2006), and this is shown to peak at $z \sim 0.5$ as illustrated in Fig. 12. In the following subsections we utilize the weight function $\phi(z)$ presented in Fig. 12 to map specific examples of theoretical models on to our parameter space, by evaluating equation (22). However as stressed earlier, we do not aim to place rigorous parameter constraints on any particular family of models.

8.1 *f*(*R*)

A more general form of the Einstein–Hilbert action replaces the Ricci scalar R with an arbitrary function $f(R)$ such that

$$S = \int f(R)\sqrt{-g}\, \mathrm{d}^4 x, \tag{24}$$

where g is the determinant of the metric tensor. This defines the broad class of $f(R)$ models. One of the most difficult tasks for any modified gravity model attempting to replace dark energy is to satisfy the stringent Solar system constraints, and most natural choices of the function $f(R)$ fail to do so. The subset of $f(R)$ models which have attracted interest are those which employ the so-called chameleon mechanism, where departures from GR are strongly suppressed in regions where R is large, only emerging when R is sufficiently small. Our location within the potential well of the Sun and the Milky Way halo may be sufficient to shield us from this unusual gravitational behaviour.

For a particular subset of $f(R)$ models which are capable of satisfying Solar system tests, the departure from GR may be characterized as (Zhao et al. 2012)

$$\mu(k, a) = \frac{1}{3 + 3(aM/k)^2}, \tag{25}$$

where the scalaron mass $M(a) = 1/\sqrt{3\,\mathrm{d}^2 f/\mathrm{d}R^2}$. For any given redshift and wavenumber, the value of μ lies in the range $0 \le \mu < \frac{1}{3}$. This generically enhances growth, so we expect this family of models to lie vertically above the point (0, 0) in Fig. 5. We parametrize $M = M_0 a^{-\sigma}$ and take as an example $M_0 = 0.02\,h\,\mathrm{Mpc}^{-1}$ and $\sigma = 3$, corresponding to the type of model explored in Zhao et al. (2012). In $f(R)$ models the lensing potential for a given mass distribution is unchanged from the case of GR, and so $\Sigma_0^{f(R)} = 0$. Our measure of μ is dominated by the RSD data and by evaluating equation (22) this model ought to map on to our (μ, Σ) plane at a value of $\mu_0^{f(R)} = 0.81$. This is despite $\mu(a)$ never rising above 1/3, but the stronger deviation from GR at high redshift compared to our parametrization allows a higher effective value of μ_0 to be generated. Our data therefore disfavour the more aggressive $f(R)$ models, in agreement with the findings of Zhao et al. (2012).

8.2 DGP

The higher dimensional model proposed by Dvali, Gabadadze & Porrati (2000) has proved one of the most popular gravitational models for theoretical and experimental exploration. It is of particular interest due to its physical motivation and specific observational prediction, namely a value of the growth index $\gamma = \frac{11}{16}$, or equivalently $\mu_0 = -\frac{25}{48}\Omega_\Lambda$, $\Sigma_0 = 0$. However in its most natural form there appears significant disparity with observational data (see e.g. Lombriser et al. 2009). This can be bypassed by introducing a cosmological constant, although this somewhat compromises the motivation of the DGP model.

In general the behaviour of DGP is a scale-independent suppression of the growth of structure. Like $f(R)$, the lensing potential is unaltered so $\Sigma_0^{\mathrm{DGP}} = 0$. Adopting a fiducial value $\Omega_\Lambda = 0.27$ leaves us with $\mu_0^{\mathrm{DGP}} = -0.38$. This negative value of μ remains consistent with our data.

8.3 Newtonian limit

The point at $\mu_0 = 0$, $\Sigma_0 = -0.5$ corresponds to a scenario where the present-day cosmological gravity resembles Newtonian gravity. That is, the angular deflection of light is half the value predicted by Einstein at $z = 0$, while the forces experienced by galaxies remain unchanged. This model was famously rejected in favour of GR by Dyson et al. (1920). The difference here is that we are performing this test on cosmological scales. Whether we combine our gravitational data with either BAO or the H_0 prior, the results are the same, a value of $\Sigma_0 = -0.5$ is strongly disfavoured by the data.

Another regime of interest is that of $\mu_0 < -1$, for this corresponds to the antigravitational behaviour of galaxies, in that they are repulsed from clusters and attracted towards voids. One might naively expect that if dark energy is gravitational in origin, then the repulsive nature of the expansion may also be seen within the perturbations. This region is disfavoured by the data when assuming a flat ΛCDM background, but this is no longer the case for more general backgrounds since the regime $w < -1$ permits more negative values of μ_0, as seen in the central panel of Fig. 6.

8.4 Interacting dark energy

When conducting cosmological tests of gravity, in this work and in others (Bean & Tangmatitham 2010; Daniel et al. 2010; Reyes et al. 2010; Zhao et al. 2010, 2012; Song et al. 2011; Tereno et al. 2011; Rapetti et al. 2012; Zuntz et al. 2012), we necessarily make certain assumptions such as the lack of anisotropic stress. One assumption not often made explicit is that dark energy exhibits negligible interactions with dark matter, aside from their mutual gravitational repulsion. If the two fluids were to exchange energy and momentum, this readily alters the growth of structure (Amendola 2000; Simpson 2010; Simpson, Jackson & Peacock 2011), and so could generate a false signature of modified gravity.

In the simplest interacting models, we would expect to see an alteration in the growth of large-scale structure, but no direct change to the lensing potential. Thus detecting a non-zero value of Σ_0 is a prerequisite for confirming a truly modified gravity scenario. That is to say, we cannot perform a cosmological test of gravity without gravitational lensing.

As an illustrative example, we consider the scenario of dark energy decaying into a form of dark matter. If this results in the dark matter density following a power law $\rho = \rho_0 a^{-3+\epsilon}$, the growth rate of cosmic structure is subject to a constant decrement (Simpson et al. 2011):

$$f(a) = \Omega_{\rm m}^{\gamma}(a) - \frac{67}{55}\epsilon. \tag{26}$$

Large values of ϵ lead to a significant quantity of dark energy in the early Universe, and as such are disfavoured by observations of the CMB. Taking $\epsilon = 0.01$, which is small enough not to perturb the primary anisotropies of the CMB, leads to an effective value $\mu_0^{\epsilon} = -0.99$ and $\Sigma_0^{\epsilon} = 0$, a region which is disfavoured by our results.

9 CONCLUSIONS

In this work we find no indication of a departure from GR on cosmological scales, having explored the behaviour of non-relativistic and relativistic particles in the WiggleZ, 6dFGS and CFHTLenS data. Both the motions of galaxies and the deflection of their emitted light conform to the predictions of Einstein's theory, at the level of precision permitted by current data. We place limits on our gravitational parameters $\mu_0 = 0.05 \pm 0.25$ and $\Sigma_0 = 0.00 \pm 0.14$ for a flat ΛCDM expansion history. This corresponds to deviations in the present-day time dilation and spatial curvature of $\Delta\Psi/\Psi_{\rm GR} = 0.05 \pm 0.25$ and $\Delta\Phi/\Phi_{\rm GR} = -0.05 \pm 0.3$, respectively. However, these errors are significantly correlated, as shown in Fig. 11.

For ground-based and Solar system tests, where light-travel time is short, it is relatively straightforward to conduct a geometric measurement. Cosmological experiments do not share this luxury, and considerable effort is required in order to determine the spatial positioning of the test subjects. The precision at which we map the geometry of the Universe remains one of the limiting factors in determining its gravitational potentials. This is particularly apparent when increased freedom in the cosmic expansion history is allowed, arising from a variable dark energy equation of state or non-zero global curvature. Further geometric data could be included in the analysis, such as those derived from the light curves of Type Ia supernovae. However combining a large number of data sets leaves us increasingly exposed to the effects of systematic errors. For the purposes of gravitational lensing, another source of uncertainty is the form of the matter power spectrum on non-linear scales, and this is an issue which will likely become more acute with the advent of surveys spanning a large fraction of the sky. Higher resolution *N*-body simulations can help to a certain extent, but modelling the influence of baryons may prove particularly problematic.

The absence of a compelling theoretical rival to GR makes a suitable choice of gravitational parameters rather uncertain. In order to minimize the number of degrees of freedom, and to maintain sensitivity to a broad range of models, we adopted a scale-independent modification to the Newtonian and curvature potentials. The scale dependence of our results is implicit in the wide range of sensitivities each probe possesses. The cosmic shear signal from CFHTLenS is sourced by density perturbations of the order $\sim 5\,h^{-1}$ Mpc, while the RSDs from WiggleZ involve Fourier modes with wavelengths over $30\,h^{-1}$ Mpc. Furthermore, the ISW effect causes the largest angular scales of the CMB to receive significant contributions from gravitational perturbations in excess of $\sim 500\,h^{-1}$ Mpc. If any inconsistency were seen between these results this could have been an indication of scale-dependent behaviour. Our reasons for focusing on a time-dependent variation that mimics the dominance of dark energy rather than using constant μ and Σ values are twofold. First our motivation for seeking modification to GR stems from dark energy, a phenomenon which only appears at late times. Furthermore, if we were to investigate constant μ and Σ parameters, our constraints would be dominated by the primary anisotropies of the CMB, which as shown in previous studies (Bean & Tangmatitham 2010; Zuntz et al. 2012) is consistent with a GR framework.

Solar system experiments have already eliminated many potential modifications to GR which could have provided a natural explanation for the accelerating Universe. Here we have begun to disfavour some of those which remain. While the volume of parameter space available to modified gravity models continues to shrink, the cosmological constant retains its position as the most viable solution to the dark energy problem.

ACKNOWLEDGMENTS

We would like to thank Gong-Bo Zhao, Pedro Ferreira, John Peacock, Benjamin Joachimi and the referee Joe Zuntz for helpful discussions.

This work is based on observations obtained with MegaPrime/MegaCam, a joint project of CFHT and CEA/DAPNIA, at the Canada–France–Hawaii Telescope (CFHT) which is operated by the National Research Council (NRC) of Canada, the Institut National des Sciences de l'Univers of the Centre National de la Recherche Scientifique (CNRS) of France and the University of Hawaii. This research used the facilities of the Canadian Astronomy Data Centre operated by the National Research Council of Canada with the support of the Canadian Space Agency. We thank the CFHT staff for successfully conducting the CFHTLS observations and in particular Jean-Charles Cuillandre and Eugene Magnier for the continuous improvement of the instrument calibration and the ELIXIR detrended data that we used. We also thank TERAPIX for the quality assessment and validation of individual exposures during the CFHTLS data acquisition period, and Emmanuel Bertin for developing some of the software used in this study. CFHTLenS data processing was made possible thanks to significant computing support from the NSERC Research Tools and Instruments grant program, and to HPC specialist Ovidiu Toader. The *N*-body simulations used in this analysis were performed on the TCS supercomputer at the SciNet HPC Consortium. SciNet is funded by the Canada Foundation for Innovation under the auspices of Compute Canada, the Government of Ontario, Ontario Research Fund – Research Excellence and the University of Toronto. The early stages of the CFHTLenS project were made possible thanks to the support of the European CommissionÕs Marie Curie Research Training Network DUEL (MRTN-CT-2006-036133) which directly supported members of the CFHTLenS team (LF, H. Hildebrandt, BR, MV) between 2007 and 2011 in addition to providing travel support and expenses for team meetings.

FS, CH, H. Hoekstra and BR acknowledge support from the European Research Council under the EC FP7 grant numbers 240185 (FS, CH), 279396 (H. Hildebrandt) and 240672 (BR). CB acknowledges the support of the Australian Research Council through the award of a Future Fellowship. LVW acknowledges support from the Natural Sciences and Engineering Research Council of Canada (NSERC) and the Canadian Institute for Advanced Research (CIfAR, Cosmology and Gravity program). TE is supported by the Deutsche Forschungsgemeinschaft through project ER 327/3-1 and the Transregional Collaborative Research Centre TR 33 'The Dark Universe'. H. Hildebrandt is supported by the Marie Curie IOF 252760 and by a CITA National Fellowship. H. Hoekstra also acknowledges support from Marie Curie IRG grant 230924 and the Netherlands Organisation for Scientic Research grant number 639.042.814. TDK acknowledges support from a Royal Society University Research Fellowship. YM acknowledges support from CNRS/INSU (Institut National des Sciences de l'Univers) and the Programme National Galaxies et Cosmologie (PNCG). LF acknowledges support from NSFC grants 11103012 and 10878003, Innovation Program 12ZZ134 and Chen Guang project 10CG46 of SMEC and STCSM grant 11290706600. MJH acknowledges support from the Natural Sciences and Engineering Research Council of Canada (NSERC). TS acknowledges support from NSF through grant AST-0444059-001, SAO through grant GO0-11147A and NWO. MV acknowledges support from the Netherlands Organisation for Scientific Research (NWO) and from the Beecroft Institute for Particle Astrophysics and Cosmology.

Author contributions: all authors contributed to the development and writing of this paper. The authorship list reflects the lead authors of this paper (FS, CH, DP, CB, MK) followed by two alphabetical groups. The first alphabetical group includes key contributors to the science analysis and interpretation in this paper, the founding core team and those whose long-term significant effort produced the final CFHTLenS data product. The second group covers members of the CFHTLenS team who made a significant contribution to either the project, this paper or both. CH and LVW co-led the CFHTLenS collaboration.

REFERENCES

Alcock C., Paczynski B., 1979, Nat, 281, 358
Amendola L., 2000, Phys. Rev. D, 62, 043511
Amendola L., Kunz M., Sapone D., 2008, J. Cosmol. Astropart. Phys., 4, 13
Anderson L. et al., 2012, arXiv e-prints (arXiv:1203.6594)
Ballinger W. E., Peacock J. A., Heavens A. F., 1996, MNRAS, 282, 877
Bartelmann M., Schneider P., 2001, Phys. Rep., 340, 291
Bean R., Tangmatitham M., 2010, Phys. Rev. D, 81, 083534
Benjamin J. et al., 2012, MNRAS, submitted
Bertotti B., Iess L., Tortora P., 2003, Nat, 425, 374
Bertschinger E., 2006, ApJ, 648, 797
Beutler F. et al., 2011, MNRAS, 416, 3017
Beutler F. et al., 2012, MNRAS, 423, 3430
Blake C. et al., 2011, MNRAS, 418, 1725
Blake C. et al., 2012, MNRAS, 425, 405
Clifton T., Ferreira P. G., Padilla A., Skordis C., 2012, Phys. Rep., 513, 1
Daniel S. F., Linder E. V., Smith T. L., Caldwell R. R., Cooray A., Leauthaud A., Lombriser L., 2010, Phys. Rev. D, 81, 123508
Doré O. et al., 2007, arXiv e-prints (arXiv:0712.1599)
Drinkwater M. J. et al., 2010, MNRAS, 401, 1429
Dvali G., Gabadadze G., Porrati M., 2000, Phys. Lett. B, 485, 208
Dyson F. W., Eddington A. S., Davidson C., 1920, Philos. Trans. R. Soc. Lond. Ser. A, 220, 291
Einstein A., 1916, Ann. Phys., 354, 769
Eisenstein D. J., Hu W., 1998, ApJ, 496, 605
Erben T. et al., 2009, A&A, 493, 1197
Ferreira P. G., Skordis C., 2010, Phys. Rev. D, 81, 104020
Gilbank D. G., Gladders M. D., Yee H. K. C., Hsieh B. C., 2011, AJ, 141, 94
Guzzo L. et al., 2008, Nat, 451, 541
Harnois-Déraps J., Vafaei S., Van Waerbeke L., 2012, MNRAS, 426, 1262
Hawkins E. et al., 2003, MNRAS, 346, 78
Heymans C., White M., Heavens A., Vale C., van Waerbeke L., 2006, MNRAS, 371, 750
Heymans C. et al., 2012, MNRAS, 427, 146
Hildebrandt H. et al., 2012, MNRAS, 421, 2355
Hojjati A., Pogosian L., Zhao G.-B., 2011, J. Cosmol. Astropart. Phys., 8, 5
Hudson M. J., Turnbull S. J., 2012, ApJ, 751, L30
Jain B., Vikram V., Sakstein J., 2012, arXiv e-prints (arXiv:1204.6044)
Jennings E., Baugh C. M., Pascoli S., 2011, MNRAS, 410, 2081
Joachimi B., Mandelbaum R., Abdalla F. B., Bridle S. L., 2011, A&A, 527, A26
Jones D. H. et al., 2004, MNRAS, 355, 747
Jones D. H. et al., 2009, MNRAS, 399, 683
Kaiser N., 1987, MNRAS, 227, 1
Kilbinger M., Benabed K., Cappe O., Cardoso J.-F., Fort G., Prunet S., Robert C. P., Wraith D., 2011, arXiv e-prints (arXiv:1101.0950)
Kilbinger M. et al., 2012, MNRAS, submitted
Komatsu E., Seljak U., 2002, MNRAS, 336, 1256
Komatsu E. et al., 2011, ApJS, 192, 18
Larson D. et al., 2011, ApJS, 192, 16
Lewis A., Challinor A., Lasenby A., 2000, ApJ, 538, 473
Linder E. V., 2005, Phys. Rev. D, 72, 043529
Linder E. V., Cahn R. N., 2007, Astropart. Phys., 28, 481
Lombriser L., Hu W., Fang W., Seljak U., 2009, Phys. Rev. D, 80, 063536
McDonald P., Trac H., Contaldi C., 2006, MNRAS, 366, 547
Martin D. C. et al., 2005, ApJ, 619, L1
Matsubara T., Suto Y., 1996, ApJ, 470, L1
Mehta K. T., Cuesta A. J., Xu X., Eisenstein D. J., Padmanabhan N., 2012, arXiv e-prints (arXiv:1202.0092)
Miller L. et al., 2013, MNRAS, in press
Padmanabhan N., Xu X., Eisenstein D. J., Scalzo R., Cuesta A. J., Mehta K. T., Kazin E., 2012, arXiv e-prints (arXiv:1202.0090)
Peacock J. A. et al., 2001, Nat, 410, 169
Rapetti D., Blake C., Allen S. W., Mantz A., Parkinson D., Beutler F., 2012, arXiv e-prints (arXiv:1205.4679)
Reid B. A. et al., 2012, MNRAS, 426, 2719
Reyes R., Mandelbaum R., Seljak U., Baldauf T., Gunn J. E., Lombriser L., Smith R. E., 2010, Nat, 464, 256
Riess A. G. et al., 2011, ApJ, 730, 119
Samushia L. et al., 2012, arXiv e-prints (arXiv:1206.5309)
Schrabback T. et al., 2010, A&A, 516, A63
Semboloni E., Hoekstra H., Schaye J., van Daalen M. P., McCarthy I. G., 2011, MNRAS, 417, 2020
Seo H.-J., Eisenstein D. J., 2003, ApJ, 598, 720
Sharp R. et al., 2006, Proc. SPIE, 6269
Simpson F., 2010, Phys. Rev. D, 82, 083505
Simpson F., Bridle S., 2006, Phys. Rev. D, 73, 083001
Simpson F., Peacock J. A., 2010, Phys. Rev. D, 81, 043512
Simpson F., Jackson B., Peacock J. A., 2011, MNRAS, 411, 1053
Smith R. E. et al., 2003, MNRAS, 341, 1311

Song Y.-S., Zhao G.-B., Bacon D., Koyama K., Nichol R. C., Pogosian L., 2011, Phys. Rev. D, 84, 083523
Spergel D. N. et al., 2007, ApJS, 170, 377
Tereno I., Semboloni E., Schrabback T., 2011, A&A, 530, A68
Wang L., Steinhardt P. J., 1998, ApJ, 508, 483
White M., Kochanek C. S., 2001, ApJ, 560, 539
York D. G. et al., 2000, AJ, 120, 1579
Zhang P., Liguori M., Bean R., Dodelson S., 2007, Phys. Rev. Lett., 99, 141302
Zhao G.-B., Pogosian L., Silvestri A., Zylberberg J., 2009, Phys. Rev. Lett., 103, 241301
Zhao G.-B., Giannantonio T., Pogosian L., Silvestri A., Bacon D. J., Koyama K., Nichol R. C., Song Y.-S., 2010, Phys. Rev. D, 81, 103510
Zhao G.-B., Li H., Linder E. V., Koyama K., Bacon D. J., Zhang X., 2012, Phys. Rev. D, 85, 123546
Zuntz J., Baker T., Ferreira P. G., Skordis C., 2012, J. Cosmol. Astropart. Phys., 6, 32

APPENDIX A: TREATMENT OF THE CMB

In our analysis we use the $\ell \geq 100$ *WMAP*7 data from the C_ℓ^{TT} and C_ℓ^{TE} power spectra to constrain geometric cosmological parameters, as well as a benchmark for the amplitude of matter perturbations. In contrast, the $\ell < 100$ multipoles provide additional information on the gravitational potentials through the ISW. Discarding the low multipoles would severely compromise our ability to constrain the primordial amplitude of density perturbations. This is because on small angular scales there is a strong degeneracy between the optical depth τ and the amplitude A_s, since both parameters induce a simple scaling of the amplitude. To circumvent this problem we first run a likelihood analysis on the low multipoles $2 \leq \ell < 100$, marginalizing over our full parameter set including μ_0 and Σ_0. This establishes a prior on τ, which we then use in our analysis of the data, except in those cases where the low multipoles are included. Despite the addition of modified gravity parameters, we find little degradation in the constraint on τ compared to the standard *WMAP*7 result which assumes GR. This is due to the unique signature left by τ at the large scales of the C_ℓ^{TE} spectrum, which cannot be replicated by the other parameters.

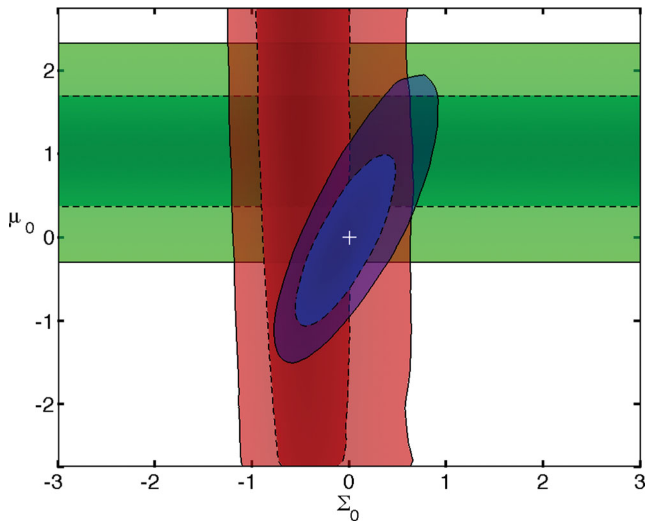

Figure A1. Constraints on our modified gravity parameters μ_0 and Σ_0 from RSDs (green), weak lensing (red) and combined (blue) for a flat ΛCDM background. A prior on H_0 is included, but there is no additional information from the CMB. The dashed contours represent the 68 and 95 per cent confidence intervals, while the cross denotes the prediction of GR.

To illustrate the impact of removing the *WMAP*7 data, we present in Fig. A1 the results for CFHTLenS $+H_0$ in red, and WiggleZ $+H_0$ in green. The substantial degradation in these contours highlights the importance of including the high-ℓ data.

This paper has been typeset from a TEX/LATEX file prepared by the author.